Stable Seawater Oxidation at High Salinity Condition Promoted by Low Iron Doped Non-Noble-Metal Electrocatalysts

Dina Zhang[1,+], Hao Cheng[2,+], Xiaoyu Hao[1], Qian Sun[1], Tianyi Zhang[1], Xinwu Xu[1], Zelin Ma[1], Tong Yang[2], Jun Ding[4], Xuqing Liu[1,*], Ming Yang[2,*], Xiaolei Huang[3,*]

1 State Key Laboratory of Solidification Processing, Center of Advanced Lubrication and Seal Materials, Northwestern Polytechnical University, Xi'an, Shaanxi 710072, P. R. China.

2 Department of Applied Physics, The Hong Kong Polytechnic University, Hung Hom, Kowloon, Hong Kong SAR, China.

3 Institute of Material and Chemistry, Ganjiang Innovation Academy, Chinese Academy of Sciences, Ganzhou, 341000, China.

4 Department of Materials Science and Engineering, National University of Singapore, Singapore 117576, Singapore.

5 Research Centre on Data Sciences & Artificial Intelligence, The Hong Kong Polytechnic University, Hung Hom, Kowloon, Hong Kong SAR, China.

*Correspondence to: xlhuang@gia.cas.cn (X.H); kevin.m.yang@polyu.edu.hk (M.Y.), or xqliu@nwpu.edu.cn (X.Q.L.).

Abstract

Electrocatalytic seawater splitting offers a promising avenue for the cost-effective and environmentally friendly hydrogen production. However, the activity of catalysts has significantly degraded at the high salinity condition, preventing commercial-scale practical applications. Here, we demonstrate that iron-doped nickel-based electrocatalysts with low doping concentration exhibit outstanding performance for the oxygen evolution reaction (OER) in seawater, particularly at high salinity condition. Notably, the OER catalysts present only a marginal increase in overpotential of approximately 5 mV as the sodium chloride concentration in the electrolyte increases from 0 M to saturation. Furthermore, the low iron-doped electrocatalysts sustain consistent oxygen generation over 100 hours of operation in a saturated seawater electrolyte. Supported by first-principles calculations, we unravel that low-concentration iron doping in Ni-based catalysts can mitigate chloride ion adsorption, thereby amplifying OER activity in saturated seawater electrolytes, which is in contrast with high iron-doped electrocatalysts. Our work provides a useful perspective on designing catalysts for electrolytic seawater OER, potentially paving the way for large-scale implementation of seawater splitting technologies.

Keywords

Non-noble-metal electrocatalyst; oxygen evolution reaction; high salinity condition; seawater splitting; hydrogen production

Introduction

Hydrogen is widely recognized as a renewable and clean energy source due to its high gravimetric energy density and pollution-free emission.[1-11] Water electrolysis presents a promising approach for hydrogen production, as a means to store intermittent solar and wind energy.[12-14] However, implementing electrocatalytic water splitting on a commercial scale remains a grand challenge, primarily due to the dependency on naturally scarce high-purity water as a raw material.[15, 16] Considerable efforts have been dedicated to producing hydrogen using the electrolysis of desalinated seawater, which requires high-purity water. However, this process is energy-intensive.[17] To put it in perspective, the global hydrogen consumption currently stands at 70 megatons per year. If seawater were to be used for hydrogen production, it would necessitate approximately 2.1 billion kilowatt-hours of electrical energy for desalination.[18,19] In this regard, direct seawater splitting emerges as an appealing, feasible, and cost-effective strategy for hydrogen production. This method bypasses the need for energy-intensive desalination processes, thereby significantly enhancing the efficiency and sustainability of hydrogen production from seawater.

Various investigations have been conducted to develop electrocatalysts for the oxygen evolution reaction (OER) in seawater with low salt concentration (approximately 0.6 M sodium chloride) and alkaline electrolyte. The alkaline environment is preferred as it can suppress the evolution of chlorine gas.[20] However, it has been observed that the activity of OER catalysts degrades rapidly in seawater electrolyte due to the corrosive effects of chloride ions (Cl-) on the catalytic electrode.[21,

[22] Additionally, the chloride ion concentration rises proportionally as seawater gets consumed during the OER process. This increase in chloride ions can obstruct the active sites of the catalyst and reduce the number of water molecules or hydroxide ions on the catalyst surface, thereby leading to a decline in catalytic performance.[23-29] As such, maintaining high catalytic activity and stability during direct seawater electrolysis proves challenging[30, 31]. Hence, the development of a catalyst that demonstrates both high activity and stability in high-salinity seawater is of paramount importance for the successful realization of large-scale seawater splitting processes.

In this study, we present novel findings on the electrocatalytic performance of a non-noble-metal nickel-based catalyst doped with a low concentration of iron (Fe-NiO_xH_y/CC) over a wide range of salt concentrations in the electrolyte. Our results demonstrate that Fe-doped NiO_xH_y/CC catalysts at low doping concentration exhibits superior electrochemical activity, with an overpotential of ~201 mV (at 0 M salt in 1 M KOH) and ~206 mV (at saturated salt in 1 M KOH) at a current density of 10 mA cm^{-2}. Furthermore, the Fe-NiO_xH_y/CC catalyst exhibits remarkable stability, maintaining its electrocatalytic activity for up to 100 hours in a saturated alkaline seawater electrolyte. Our density functional theory (DFT) calculations indicate that the improved catalytic performance can be attributed to the presence of Fe-Ni bridge sites in the catalyst, which can modulate Cl* adsorption and thus lead to high OER activity. These findings provide useful insights into the design of efficient and stable electrocatalysts for seawater splitting.

Results and discussions

The synthesis process of the Fe-NiO_xH_y/CC electrocatalyst is illustrated in Figure 1, where a black carbon cloth (CC) is used as the conductive substrate (Figure 1a). Nickel metal doped with ~6 mol% iron was electrochemically deposited on the carbon cloth (NiFe/CC), as shown in Figure 1b. The surface roughness of NiFe/CC increases significantly compared to the black carbon cloth. Elemental mapping using the corresponding X-ray energy dispersive spectroscopy (EDS) shows that Fe and Ni are uniformly distributed across the entire carbon cloth (Figure S1, Supporting Information). The composition and structure of NiFe/CC were revealed by the XRD pattern and XPS spectrum (Figures 2a and 2b). The XRD patterns of NiFe/CC exhibit three peaks at 44.5°, 51.8°, and 76.3°, corresponding to (111), (200), and (220) planes of cubic Ni (PDF # 70-0989),[32] respectively, indicating the formation of metal nickel on the carbon cloth.[33] The Ni 2p XPS spectrum (Figure 2b) shows Ni $2p_{3/2}$ and $2p_{1/2}$ peaks at 855.8 eV and 873.7 eV, respectively, corresponding to Ni^{2+},[34] along with zero-valent Ni peak at 851.9 eV. The Fe 2p XPS spectra (Figure 2c) show two significant peaks of the $2p_{3/2}$ and $2p_{1/2}$ components at 712.8 eV and 724.3 eV, with a peak distance of ~12 eV, confirming the presence of Fe^{3+}.[35] The O 1s XPS spectrum (Figure 2d) exhibits a characteristic peak of hydroxy-oxygen at 531.4 eV derived from $Ni(OH)_2$ and $Fe(OH)_3$.[36] These results suggest that the deposited NiFe/CC has a mixture structure of $Ni(OH)_2$ and $Fe(OH)_3$.

Through surface treatment, the electronic structure of the active site can be modulated in the sulfur polyanion environment, leading to high OER activity.[37, 38] After the sulphuration on NiFe/CC, metal nickel can still be detected (Figure 2a), and the Ni

2p spectrum shows the presence of both Ni^{2+} and Ni^{0} in the sulfurized NiFe/CC (Figure 2b).[39, 40] Figure 2c shows the XPS spectrum of Fe 2p in the sulfurized NiFe/CC, which indicates Fe^{3+} oxidation state. The XPS spectrum of O 1s (Figure 2d) shows the presence of the hydroxy-oxygen after the sulphuration. However, the intensity of hydroxy-oxygen peak decreases in this sulfurized sample. In addition, the XPS spectrum of S 2p shows three peaks that result from the superposition of the S^{2-}, S_2^{2-}, and S_n^{2-} peaks (Figure S2, Supporting Information).[41]

To further improve the catalyst performance, the sulfurized NiFe/CC sample was treated by using electrochemical oxidation, which leads to the formation of a lamellar hydroxide structure (Figure 1c). This alkaline oxidation process facilitates the conversion of Ni sites into disordered NiOOH on the electrode surface.[42] The hydrothermal sulphuration and electrochemical oxidation processes contribute to increasing the active surface area of the catalyst and transforming the nickel-ferric hydroxide composites into active substances. The structural characterization of the synthesized Fe-NiO_xH_y/CC is depicted in Figure 3. The Raman spectrum of Fe-NiO_xH_y/CC reveals Ni^{III}-O vibration peaks at 471 cm^{-1} and 551 cm^{-1}, as shown in Figure 3a.[43] These results suggest the presence of active species NiOOH .[44] The sample remains amorphous, as confirmed by the XRD pattern in Figure S3 of the Supplementary Information.[45] XPS was employed to further investigate the surface electronic states of Fe-NiO_xH_y/CC composites. As shown in Figure 3b, the peaks at 855.6 eV and 873.3 eV in the Ni 2p spectrum of Fe-NiO_xH_y/CC could be assigned to Ni^{3+} $2p_{3/2}$ and Ni^{3+} $2p_{1/2}$, respectively. The Ni^{3+} 2p peaks could potentially signify the

formation of NiOOH.[46] The XPS spectrum of Fe 2p confirms the presence of Fe^{3+} (Figure. 3c).[35] Two peaks are observed at 529.5 eV and 530.6 eV (Figure. 3d) for the O 1s spectrum of Fe-NiO_xH_y/CC catalyst, with the former corresponding to the binding energy of M-O and the latter corresponding to the M-OH.[47, 48] This suggests that the sample is in a mixed state of NiOOH, FeOOH, and $Ni(OH)_2$,[49] which are unstable during the reaction due to mutual transformation[43]. The XPS measurement on S 2p suggests that there is no S in the sample after oxidation (Figure S4, Supporting Information). In addition, the relative contents of each element in Fe-NiO_xH_y/CC were determined by inductively coupled plasma optical emission spectrometry (ICP-OES). According to the results of the calculation, the Fe/Ni molar mass ratios in Fe-NiO_xH_y are found to be approximately 6 mol%.

To explore the OER performance of Fe-NiO_xH_y/CC, the three-electrode system was used, with NiO_xH_y/CC (Figure S5, Supporting information) and $Ni(OH)_2$ (Figure S6, Supporting information) as the referential samples. Figure 4a shows the polarization curves of various catalysts in 1M KOH electrolyte. Among them, the Fe-NiO_xH_y/CC exhibits the highest OER activity, with a low overpotential of ~201 mV at a current density of 10 mA cm^{-2}, which is significantly lower than that of the NiO_xH_y/CC (~215 mV) and $Ni(OH)_2$/CC (~279 mV) (Figure 4b). To further demonstrate the catalytic performance of the materials, we investigated the corresponding Tafel plots of all the catalysts (Figure 4c). Fe-NiO_xH_y/CC shows a smaller Tafel slope (50 mV dec^{-1}) compared to those of NiO_xH_y/CC (140 mV dec^{-1}) and $Ni(OH)_2$ (133 mV dec^{-1}). The small Tafel slope indicates a faster increment of OER rate with increasing overpotential,

leading to higher catalytic activity.[50, 51] These results demonstrate that doping Fe can significantly enhance the OER performance of Ni-based catalysts.

Next, we examine the stability of the electrocatalyst. As Figure 4d shows, Fe-NiO_xH_y/CC exhibits enhanced catalytic stability in comparison to NiO_xH_y/CC (Figure S7, Supporting information) and $Ni(OH)_2$/CC (Figure S8, Supporting information) across a range of conditions, from 0.6 M NaCl alkaline electrolyte to saturated NaCl alkaline electrolyte. To elucidate the impact of Cl- on the Fe-NiO_xH_y/CC electrocatalyst, we evaluated the performance of the sample under varying salt concentrations using chronopotentiometry measurements. Figure 4e summarizes the overpotentials required for Fe-NiO_xH_y/CC as an OER electrocatalyst to drive current densities of 10 mA cm^{-2} in 0.6 M NaCl alkaline electrolytes, 2 M NaCl alkaline electrolytes, and saturated NaCl alkaline electrolytes. They are observed to be 202 mV, 208 mV and 206 mV, respectively. The marginal overpotential difference (~4 mV) between 0.6 M NaCl alkaline electrolyte and saturated NaCl alkaline electrolyte suggests that the performance of the Fe-NiO_xH_y/CC sample remains unaffected by varied chloride ion concentrations. We further performed a comparative analysis of Fe-NiO_xH_y/CC, NiO_xH_y/CC and $Ni(OH)_2$/CC samples in 0 M NaCl alkaline electrolyte, 0.6 M NaCl alkaline electrolyte, 2 M NaCl alkaline electrolyte and saturated NaCl alkaline electrolyte, as shown in in Figure 4f and Figure 4g. In the four electrolyte concentrations, the overpotential growth trend is different for Fe-NiO_xH_y/CC, NiO_xH_y/CC, and $Ni(OH)_2$/CC. For the NiO_xH_y/CC, the η_{10} (the overpotential at the current density of 10 mA cm^{-2}) values are 215 mV, 214 mV, 219 mV, and 230 mV,

respectively, with a maximum differences of ~16 mV, whereas for $Ni(OH)_2$/CC, the η_{10} values are 279 mV, 286 mV, 290 mV, and 306 mV, respectively, with a maximum differences of ~27 mV. In contrast, the maximum overpotential difference of Fe-NiO_xH_y/CC catalyst is only ~5 mV in the various salt concentrations, much smaller than those of NiO_xH_y/CC and $Ni(OH)_2$/CC catalysts. This suggests that the low Fe-doping concentration contributes to the enhanced stability of the OER activity, even with varying salt concentrations from 0 M to saturated levels. Furthermore, Figure S9 in the Supporting Information illustrates that Fe-NiO_xH_y/CC not only performs excellently but also exhibits remarkable stability under high salt concentrations. Figures 4h and 4i demonstrate the catalytic stability of the Fe-NiO_xH_y/CC catalyst in an alkaline seawater electrolyte. The Fe-NiO_xH_y/CC catalyst maintains stable catalytic performance for up to 12 hours at 10 mA cm^{-2} in seawater electrolyte (0.6 M seawater salt in 1 M KOH), as shown in Figure 4h. In saturated alkaline seawater electrolyte, the catalyst with low Fe doping retains high stability up to 100 hours of continuous reaction, as depicted in Figure 4i.

To evaluate the impact of iron content on the performance of the catalyst, we carried out an experimental investigation on the linear sweep voltammetry (LSV) performance of samples prepared with varying molar ratios of iron to nickel (Fe/Ni) under conditions of saturated salt concentration. Our results demonstrated that catalysts with a Fe/Ni ratio of ~ 6 mol% outperforms those with Fe/Ni ratios of ~ 1 mol%, ~ 3 mol%, ~ 45 mol%, and 1000 mol%. This indicates that the presence of nickel-iron bridge sites within the catalysts can enhance performance, whereas performance tends

to decrease when these bridge sites are exclusively nickel-nickel or iron-iron. Consequently, catalysts with a lower iron content exhibit superior catalytic performance (Figure S10, Supporting Information). These results align well with theoretical simulation findings, as detailed subsequently.

In order to elucidate the underlying mechanism responsible for the enhanced performance of the Fe-NiO_xH_y/CC catalyst, we conducted density functional theory (DFT) calculations. OER is known to evolve several elementary steps, where the "*" symbol denotes the relevant intermediate absorbent states.[52] As illustrated in Figure 5a, the overpotential of the reaction can be estimated by the calculated free energy of the OH*, O*, and OOH* intermediates.[53] Establishing a correlation between the free energy of intermediates and the overpotential of reactions is crucial for the rational design of catalysts.[54] Figure 5b presents the adsorption energies of OER and Cl^* intermediates at Ni and Fe surface sites for pure NiOOH with Ni-Ni bridge site, FeOOH with Fe-Fe bridge site, and Fe doped NiOOH model structures with Fe-Ni bridge site. The calculated results suggest that the pure NiOOH and FeOOH structures display the strongest and weakest adsorption capacity towards OER and Cl^* intermediates, respectively. The slightly doped Fe-NiOOH structure exhibits a moderate adsorption capacity. Furthermore, we calculated the Gibbs free energies of the proposed OER pathway with OH*, O*, and OOH* intermediates and estimated the OER overpotentials in Figure 5c. Compared with pure NiOOH and FeOOH structures, Fe-Ni bridge sites in Fe-NiOOH show a lower OER overpotential, implying that Fe-doped Ni sites are more favorable for OER than pure Ni and Fe sites. This suggests that Fe-NiO_xH_y/CC samples

possess low overpotential and moderate adsorption capacity for both OER and Cl^* intermediates. According to the linear scaling relations in Figure 5b, the OER overpotential can be determined by the free energy of O* intermediate (ΔG (O*)) and its energy difference to HO* intermediate, denoting as ΔG (O*) -ΔG (HO*).[55] Figure 5d depicts the two-dimensional OER activity volcano, representing the overpotential as a function of Gibbs free energies of OER intermediates. It clearly shows that the Fe-NiO_xH_y/CC has the lowest OER overpotential compared to the NiOOH and FeOOH structures. These results demonstrate that Ni-Fe bridges in catalysts are favorable for a low OER overpotential and moderated adsorption energies of Cl^-, leading to high catalytic activity for Fe-NiO_xH_y/CC in salt concentrations varying from 0 M to saturated alkaline electrolyte (Figure S10, Supporting information). The atomic composition of Fe-NiO_xH_y can be visually assessed from the aberration-corrected transmission electron microscopy (AC-TEM) image. As depicted in Figure S12, the elements Ni and Fe exhibit a uniform distribution, which implies the presence of abundant Fe-Ni bridging sites, and thus supports the DFT calculations.

Conclusion

In conclusion, we have successfully prepared Fe-NiO_xH_y/CC catalysts with a low iron content of about 6 mol%, which demonstrates excellent OER performance. The Fe-NiO_xH_y/CC catalyst exhibits a low overpotential of only ~201 mV at 10 mA cm^{-2} and outstanding stability in alkaline electrolyte. Moreover, the overpotential variation attenuation of the catalyst is only ~5 mV when the salt concentration in the electrolyte increases from 0 M to saturated NaCl alkaline electrolyte, and the Fe-NiO_xH_y/CC

catalyst can be stable for at least 100 h. Combined with density functional theory calculations, it turns out that the low Fe doping weakens the adsorption of chloride ions on the OER catalyst in saturated seawater electrolyte while enhancing its activity. These findings demonstrate that the Fe-NiO_xH_y/CC has the potential as a high-performance electrocatalyst at high salt concentrations. Our work provides a new perspective on designing electrocatalysts with improved stability and salt tolerance for seawater splitting and large-scale hydrogen production.

Experiment Section

Synthesis of NiO_xH_y/CC, Fe-NiO_xH_y/CC. First, carbon cloth (1×2 cm^2) was roasted in a tubular furnace into for 15 minutes at 450 ℃ to make carbon cloth became hydrophilic. The Fe-NiO_xH_y/CC nanosheet arrays were prepared through a simple, convenient electrodeposition method and hydrothermal method. To prepare the Fe-NiO_xH_y/CC catalyst, 0.075 mmol $NiSO_4 \cdot 6H_2O$, 0.6 mmol H_3BO_3, and 0.0042 mmol $Fe_2(SO_4)_3$ were dissolved in 50 mL of DI water, the solution was dispersed evenly. The electrodeposition process was finished via a three-electrode system, a graphite paper sheet was used as the auxiliary electrode, whereas an Hg/HgO electrode was selected as the reference electrode. Also, the treated carbon cloth (1×2 cm^2) was used as the working electrode, and the 50 mL solution prepared as mentioned above was used as the electrolyte solution. The electrodeposition current was -10 mA cm^{-2} versus Hg/HgO electrode, and the electrodeposition time was 1 hour. The prepared electrocatalyst was washed by DI water and dried for 5 minutes. The experiment was carried out at room temperature.

Secondly, to sulphurate the prepared electrocatalyst, 0.05 g sulfur powder was dissolved into 10 mL oleylamine, and then the prepared electrocatalyst carbon cloth (1×2 cm^2) was placed into the solution, The solution was transferred to a Teflon-lined PTFE autoclave vessel and heated at 150 °C for 5 h. the prepared carbon cloth of sulphuration was washed several times in a solution with a volume ratio of 1:1 ethanediamine and ethanol.

Finally, the prepared carbon cloth of sulphuration was electrochemical oxidation at 10mA cm^{-2} for 1h. The preparation process of the NiO_xH_y/CC catalyst is the same as above, and other conditions remain unchanged; the only change is that without $Fe_2(SO_4)_3$ is added.

Synthesis of Ni(OH)₂/CC. $Ni(OH)_2$/CC catalyst were prepared through a simple hydrothermal method. 4 mmol NH_4Cl and 2.8 mmol $Ni(NO_3)_2$ were dissolved in 40 mL of DI water , then the solution was dispersed evenly. The carbon cloth was soaked in the prepared solution. The solution was transferred to a Teflon-lined PTFE autoclave vessel and heated at 120 °C for 6 h. Carbon cloth was washed several times and dried.

Material Characterization. D8 Advance Power X-ray diffractometer (XRD) was performed to characterize the crystal structure date of the samples, with high-intensity Cu-Kα radiation (λ = 0.15 nm), and the scanning range was 10−80°. The scanning rate was 5° min^{-1}. Scanning electron microscope (SEM) was used (FEI Helios G4 CX with 10 kV and 43 pA working condition) to obtain the images of microscopic morphology. X-ray photoelectron spectroscopy (XPS, PHI 5000 VersaProbeIII) analysis was performed to get the chemical valence of the catalysts. Raman spectroscopy (RTS2,

Zolix) measurement was employed using a 532 nm excitation source. Inductively coupled plasma optical emission spectrometry (ICP-OES) measurement was conducted on AGILENT ICP-OES 730. Spherical aberration-corrected transmission electron microscope (AC-TEM) was used (JEM-ARM200F) to obtain the images of microscopic morphology and the corresponding elemental mapping images.

Electrochemical Testing. All electrochemical tests were conducted using a traditional three-electrode system on the CHI660E electrochemical workstation, in which the graphite paper was used as the auxiliary electrode, Hg/HgO was used as the reference electrode, and the deposited catalysts on the carbon cloth was selected as the working electrode. The salt concentrations of electrolytes were varied by dissiolving 0 M NaCl, 0.6 M NaCl, 2 M NaCl and saturated NaCl dissolved in 1M KOH solution. The whole potential was transformed into a reversible hydrogen electrode (RHE), taking advantage of the equation: E(RHE) = E(Hg/ HgO) + 0.098 + 0.059 × pH. The catalyst was activated with the linear sweep voltammetry (LSV) technique with a sweep rate of 1 mV s^{-1}. EIS analysis was obtained with a frequency between 10 mHz and 700 kHz at 0.55 V (vs Hg/HgO) for an amplitude of 5 mV to investigate the charge-transfer Capacity of the catalyst. All the polarization curves were recorded with 85% iR compensation using the solution resistance estimated from EIS results. In addition, the stability was measured using the chronopotentiometry technique which was conducted at 10 mA cm^{-2}.

Computational Methods. Density functional theory (DFT) calculations were carried out using the Quantum Espresso package and ultrasoft pseudopotentials[56, 57].

The exchange-correlation interaction was approximated by the revised Perdew–Burke–Ernzerhof (RPBE) functional.[58] The kinetic energy cutoff for plane wave expansion was set to 50 Ry. To improve the description of localized Ni and Fe *d*-electrons in the Fe-NiO_xH_y catalysts, a simplified rotationally invariant implementation[59] of Hubbard-U model was employed with a value of $\mathrm{U(Ni)} = 6.6\ \mathrm{eV}$ and $\mathrm{U(Fe)} = 3.5\ \mathrm{eV}$ as reported by Friebel et al[52] To minimize periodic interactions, a vacuum layer with a thickness of 16 Å was incorporated perpendicular to the surface of the slab model. The Brillouin zone was sampled using $4 \times 5 \times 1$ Monkhorst-Pack *k*-point grids and a Fermi-level smearing width of 0.1 eV was employed. Spin-polarization effects were considered on all calculations. All structures were optimized until force components below 0.05 eV/Å. The energies of molecules O_2 and H_2O were also calculated as the gas-phase reference. The reaction free energy was calculated as $\Delta \mathrm{G} = \Delta E_{DFT} + \Delta ZPE - T\Delta S$, where ΔE_{DFT} is the change in total energy calculated by DFT, and ΔZPE and $T\Delta S$ is the zero-point energy and entropy corrections for the gas-phase molecules taken from reference[60].

ASSOCIATED CONTENT

Supporting Information

Spherical aberration-corrected transmission electron microscope, Scan electron microscopy images, X-ray energy Spectrometer (EDS), X-ray diffraction patterns, electrochemical measurements, and detailed data tables.

AUTHOR INFORMATION

Corresponding Author

*Correspondence to: xlhuang@gia.cas.cn (X.H); kevin.m.yang@polyu.edu.hk (M.Y.), or xqliu@nwpu.edu.cn (X.Q.L.).

Authors declare no competing interests.

ACKNOWLEDGMENTS

The authors acknowledge the funding support by the the National Natural Science Foundation of China (51401084) and Natural Science Foundation of Jiangxi, China (20232ACB203002).

Reference

1. Wang, B.; Tang, C.; Wang, H.-F.; Chen, X.; Cao, R.; Zhang, Q., A Nanosized CoNi Hydroxide@Hydroxysulfide Core-Shell Heterostructure for Enhanced Oxygen Evolution. *Advanced Materials* **2019,** *31* (4), 1805658.

2. Liu, B.; Chu, W.; Liu, S.; Zhou, Y.; Zou, L.; Fu, J.; Liu, M.; Fu, X.; Ouyang, F.; Zhou, Y., Engineering the nanostructures of solution proceed $In_2Se_xS_{3-x}$ films with enhanced near-infrared absorption for photoelectrochemical water splitting. *Journal of Physics D: Applied Physics* **2022,** *55* (43), 434004.

3. Huang, X.; Wang, F.; Ma, L.; Wang, J.; Zhang, T.; Hao, X.; Chi, X.; Cheng, H.; Yang, M.; Ding, J.; Ang, D. S., Reversion of catalyst valence states for highly efficient water oxidation. *Catalysis Science & Technology* **2023,** *13* (9), 2820-2826.

4. Gao, G.; O'Mullane, A. P.; Du, A., 2D MXenes: A New Family of Promising Catalysts for the Hydrogen Evolution Reaction. *ACS Catalysis* **2016,** *7* (1), 494-500.

5. Yang, T.; Zhou, J.; Song, T. T.; Shen, L.; Feng, Y. P.; Yang, M., High-Throughput Identification of Exfoliable Two-Dimensional Materials with Active Basal Planes for Hydrogen Evolution. *ACS Energy Letters* **2020,** *5* (7), 2313-2321.

6. Khan, M. A.; Ngo, H. H.; Guo, W.; Liu, Y.; Zhang, X.; Guo, J.; Chang, S. W.; Nguyen, D. D.; Wang, J., Biohydrogen production from anaerobic digestion and its potential as renewable energy. *Renewable Energy* **2018,** *129*, 754-768.

7. Carmo, M.; Fritz, D. L.; Mergel, J.; Stolten, D., A comprehensive review on PEM water electrolysis. *International Journal of Hydrogen Energy* **2013,** *38* (12), 4901-4934.

8. Gong, M.; Wang, D.-Y.; Chen, C.-C.; Hwang, B.-J.; Dai, H., A mini review on nickel-based electrocatalysts for alkaline hydrogen evolution reaction. *Nano Research* **2015,** *9* (1), 28-46.

9. Anantharaj, S.; Ede, S. R.; Sakthikumar, K.; Karthick, K.; Mishra, S.; Kundu, S., Recent Trends and Perspectives in Electrochemical Water Splitting with an Emphasis on Sulfide, Selenide, and Phosphide Catalysts of Fe, Co, and Ni: A Review. *ACS Catalysis* **2016,** *6* (12), 8069-8097.

10. Pu, Z.; Zhao, J.; Amiinu, I. S.; Li, W.; Wang, M.; He, D.; Mu, S., A universal synthesis strategy for P-rich noble metal diphosphide-based electrocatalysts for the hydrogen evolution reaction. *Energy & Environmental Science* **2019,** *12* (3), 952-957.

11. Tian, X.; Zhao, P.; Sheng, W., Hydrogen Evolution and Oxidation: Mechanistic Studies and Material Advances. *Advanced Materials* **2019,** *31* (31), 1808066.

12. Kong, X.; Lei, J.; Cao, Q.; Liu, F.; Xie, C.; Huang, M.; Xu, X.; Wang, J., Alloy Foam‐Derived $Ni_{0.86}Fe_{2.14}O4$Hexagonal Plates as an Efficient Electrochemical Catalyst for the Oxygen Evolution Reaction. *ChemistrySelect* **2020,** *5* (4), 1578-1585.

13. Zhang, J.; Li, J.; Zhong, C.; Xi, P.; Chao, D.; Gao, D., Surface-Electronic-Structure Reconstruction of Perovskite via Double-Cation Gradient Etching for Superior Water Oxidation. *Nano Lett* **2021,** *21* (19), 8166-8174.

14. Zhong, H.-X.; Wang, J.; Zhang, Q.; Meng, F.; Bao, D.; Liu, T.; Yang, X.-Y.; Chang, Z.-W.; Yan, J.-M.; Zhang, X.-B., In Situ Coupling FeM (M = Ni, Co) with Nitrogen-Doped Porous Carbon toward Highly Efficient Trifunctional Electrocatalyst for Overall Water Splitting and Rechargeable Zn-Air Battery. *Advanced Sustainable Systems* **2017,** *1* (6), 1700020.

15. Zhou, Y.; Pondick, J. V.; Silva, J. L.; Woods, J. M.; Hynek, D. J.; Matthews, G.; Shen, X.; Feng, Q.; Liu, W.; Lu, Z.; Liang, Z.; Brena, B.; Cai, Z.; Wu, M.; Jiao, L.; Hu,

S.; Wang, H.; Araujo, C. M.; Cha, J. J., Unveiling the Interfacial Effects for Enhanced Hydrogen Evolution Reaction on MoS_2/WTe_2 Hybrid Structures. *Small* **2019,** *15* (19), 1900078.

16. Chen, S.; Duan, J.; Zheng, Y.; Chen, X.; Du, X. W.; Jaroniec, M.; Qiao, S.-Z., Ionic liquid-assisted synthesis of N/S-double doped graphene microwires for oxygen evolution and Zn–air batteries. *Energy Storage Materials* **2015,** *1*, 17-24.

17. Delpisheh, M.; Haghghi, M. A.; Athari, H.; Mehrpooya, M., Desalinated water and hydrogen generation from seawater via a desalination unit and a low temperature electrolysis using a novel solar-based setup. *International Journal of Hydrogen Energy* **2021,** *46* (10), 7211-7229.

18. Elimelech, M.; Phillip, W. A., The future of seawater desalination: energy, technology, and the environment. *science* **2011,** *333* (6043), 712-717.

19. Ji, M.; Wang, J., Review and comparison of various hydrogen production methods based on costs and life cycle impact assessment indicators. *International Journal of Hydrogen Energy* **2021,** *46* (78), 38612-38635.

20. Yu, Z. Y.; Duan, Y.; Feng, X. Y.; Yu, X.; Gao, M. R.; Yu, S. H., Clean and Affordable Hydrogen Fuel from Alkaline Water Splitting: Past, Recent Progress, and Future Prospects. *Adv Mater* **2021,** *33* (31), e2007100.

21. Khatun, S.; Roy, P., Cobalt chromium vanadium layered triple hydroxides as an efficient oxygen electrocatalyst for alkaline seawater splitting. *Chem Commun (Camb)* **2022,** *58* (8), 1104-1107.

22. Dresp, S.; Dionigi, F.; Klingenhof, M.; Merzdorf, T.; Schmies, H.; Drnec, J.; Poulain, A.; Strasser, P., Molecular Understanding of the Impact of Saline Contaminants and Alkaline pH on NiFe Layered Double Hydroxide Oxygen Evolution Catalysts. ACS Catalysis 2021, 11 (12), 6800-6809.

23. Tu, Q.; Liu, W.; Jiang, M.; Wang, W.; Kang, Q.; Wang, P.; Zhou, W.; Zhou, F., Preferential Adsorption of Hydroxide Ions onto Partially Crystalline NiFe-Layered Double Hydroxides Leads to Efficient and Selective OER in Alkaline Seawater. *ACS Applied Energy Materials* **2021,** *4* (5), 4630-4637.

24. Das, C.; Roy, P., Cobalt and iron phosphates with modulated compositions and phases as efficient electrocatalysts for alkaline seawater oxidation. *Chem Commun (Camb)* **2022,** *58* (47), 6761-6764.

25. Jiang, K.; Liu, W.; Lai, W.; Wang, M.; Li, Q.; Wang, Z.; Yuan, J.; Deng, Y.; Bao, J.; Ji, H., NiFe Layered Double Hydroxide/FeOOH Heterostructure Nanosheets as an Efficient and Durable Bifunctional Electrocatalyst for Overall Seawater Splitting. *Inorg Chem* **2021,** *60* (22), 17371-17378.

26. Hu, R.; Liu, F.; Qiu, H.; Miao, H.; Wang, Q.; Zhang, H.; Wang, F.; Yuan, J., High-Property Anode Catalyst Compositing Co-Based Perovskite and NiFe-Layered Double Hydroxide for Alkaline Seawater Splitting. *Processes* **2022,** *10* (4), 668.

27. Liu, X.; Gong, M.; Xiao, D.; Deng, S.; Liang, J.; Zhao, T.; Lu, Y.; Shen, T.; Zhang, J.; Wang, D., Turning Waste into Treasure: Regulating the Oxygen Corrosion on Fe Foam for Efficient Electrocatalysis. *Small* **2020,** *16* (24), e2000663.

28. Chen, Y.; Wang, Q. P.; Cai, C.; Yuan, Y. N.; Cao, F. H.; Zhang, Z.; Zhang, J. Q., Electrodeposition and characterization of nanocrystalline CoNiFe films. *Thin Solid Films* **2012,** *520* (9), 3553-3557.

29. Lu, X.; Zhao, C., Electrodeposition of hierarchically structured three-dimensional nickel-iron electrodes for efficient oxygen evolution at high current densities. *Nat Commun* **2015,** *6*, 6616.

29. Hu, H.; Xiao, W.; Yuan, J.; Shi, J.; He, D.; Shangguan, W., High photocatalytic activity and stability for decomposition of gaseous acetaldehyde on TiO2/Al2O3 composite films coated on foam nickel substrates by sol-gel processes. *Journal of Sol-Gel Science and Technology* **2007,** *45* (1), 1-8.

30. Shi, S.; Sun, S.; He, X.; Zhang, L.; Zhang, H.; Dong, K.; Cai, Z.; Zheng, D.; Sun, Y.; Luo, Y.; Liu, Q.; Ying, B.; Tang, B.; Sun, X.; Hu, W., Improved Electrochemical Alkaline Seawater Oxidation over Cobalt Carbonate Hydroxide Nanowire Array by Iron Doping. *Inorganic Chemistry* **2023,** *62* (30), 11746-11750.

31. Song, H. J.; Yoon, H.; Ju, B.; Lee, D.-Y.; Kim, D.-W., Electrocatalytic Selective Oxygen Evolution of Carbon-Coated Na2Co1–xFexP2O7 Nanoparticles for Alkaline Seawater Electrolysis. ACS Catalysis 2019, 10 (1), 702-709.

32. Hu, H.; Xiao, W.; Yuan, J.; Shi, J.; He, D.; Shangguan, W., High photocatalytic activity and stability for decomposition of gaseous acetaldehyde on TiO_2/Al_2O_3 composite films coated on foam nickel substrates by sol-gel processes. Journal of Sol-Gel Science and Technology 2007, 45 (1), 1-8.

33. Gao, Z.; Liu, F.; Wang, L.; Luo, F., Highly efficient transfer hydrodeoxygenation of vanillin over Sn4+-induced highly dispersed Cu-based catalyst. *Applied Surface Science* **2019,** *480*, 548-556.

34. Grosvenor, A. P.; Biesinger, M. C.; Smart, R. S. C.; McIntyre, N. S., New interpretations of XPS spectra of nickel metal and oxides. *Surface Science* **2006,** *600* (9), 1771-1779.

35. Wang, J.; Ma, X.; Qu, F.; Asiri, A. M.; Sun, X., Fe-Doped Ni_2P Nanosheet Array for High-Efficiency Electrochemical Water Oxidation. *Inorg Chem* **2017,** *56* (3), 1041-1044.

36. Liu, W.; Bao, J.; Xu, L.; Guan, M.; Lei, Y., Chromium-modulated multifunctional electrocatalytic activities of spinel oxide for Zn-air batteries and overall water splitting. *Journal of Power Sources* **2020,** *479*.

37. Zhao, C.-X.; Liu, J.-N.; Wang, C.; Wang, J.; Song, L.; Li, B.-Q.; Zhang, Q., An anionic regulation mechanism for the structural reconstruction of sulfide electrocatalysts under oxygen evolution conditions. *Energy & Environmental Science* **2022,** *15* (8), 3257-3264.

38. Chai, Y.-M.; Zhang, X.-Y.; Lin, J.-H.; Qin, J.-F.; Liu, Z.-Z.; Xie, J.-Y.; Guo, B.-Y.; Yang, Z.; Dong, B., Three-dimensional VOx/NiS/NF nanosheets as efficient electrocatalyst for oxygen evolution reaction. *International Journal of Hydrogen Energy* **2019,** *44* (21), 10156-10162.

36. Wu, Z.; Huang, X. L.; Wang, Z. L.; Xu, J. J.; Wang, H. G.; Zhang, X. B., Electrostatic induced stretch growth of homogeneous beta-Ni(OH)2 on graphene with enhanced high-rate cycling for supercapacitors. *Sci Rep* **2014,** *4*, 3669.

37. Limaye, M. V.; Chen, S. C.; Lee, C. Y.; Chen, L. Y.; Singh, S. B.; Shao, Y. C.; Wang, Y. F.; Hsieh, S. H.; Hsueh, H. C.; Chiou, J. W.; Chen, C. H.; Jang, L. Y.; Cheng, C. L.; Pong, W. F.; Hu, Y. F., Understanding of sub-band gap absorption of femtosecond-laser sulfur hyperdoped silicon using synchrotron-based techniques. *Sci Rep* **2015,** *5*, 11466.

38. Zhang, L.; Liang, J.; Yue, L.; Dong, K.; Li, J.; Zhao, D.; Li, Z.; Sun, S.; Luo, Y.; Liu, Q.; Cui, G.; Ali Alshehri, A.; Guo, X.; Sun, X., Benzoate anions-intercalated NiFe-layered double hydroxide nanosheet array with enhanced stability for electrochemical seawater oxidation. *Nano Research Energy* **2022**, 1(3), e9120028.

39. Chai, Y.-M.; Zhang, X.-Y.; Lin, J.-H.; Qin, J.-F.; Liu, Z.-Z.; Xie, J.-Y.; Guo, B.-Y.; Yang, Z.; Dong, B., Three-dimensional VOx/NiS/NF nanosheets as efficient electrocatalyst for oxygen evolution reaction. International Journal of Hydrogen Energy 2019, 44 (21), 10156-10162.

39. Han, M. H.; Pin, M. W.; Koh, J. H.; Park, J. H.; Kim, J.; Min, B. K.; Lee, W. H.; Oh, H.-S., Improving the oxygen evolution reaction using electronic structure modulation of sulfur-retaining nickel-based electrocatalysts. *Journal of Materials Chemistry A* **2021,** *9* (47), 27034-27040.

40. Wu, Z.; Huang, X. L.; Wang, Z. L.; Xu, J. J.; Wang, H. G.; Zhang, X. B., Electrostatic induced stretch growth of homogeneous beta-Ni(OH)2 on graphene with enhanced high-rate cycling for supercapacitors. Sci Rep 2014, 4, 3669.

41. Limaye, M. V.; Chen, S. C.; Lee, C. Y.; Chen, L. Y.; Singh, S. B.; Shao, Y. C.; Wang, Y. F.; Hsieh, S. H.; Hsueh, H. C.; Chiou, J. W.; Chen, C. H.; Jang, L. Y.; Cheng, C. L.; Pong, W. F.; Hu, Y. F., Understanding of sub-band gap absorption of femtosecond-laser sulfur hyperdoped silicon using synchrotron-based techniques. Sci Rep 2015, 5, 11466.

42. Zhang, L.; Li, L.; Liang, J.; Fan, X.; He, X.; Chen, J.; Li, J.; Li, Z.; Cai, Z.; Sun, S.; Zheng, D.; Luo, Y.; Yan, H.; Liu, Q.; Alshehri, A. A.; Guo, X.; Sun, X.; Ying, B., Highly efficient and stable oxygen evolution from seawater enabled by a hierarchical NiMoSx microcolumn@NiFe-layered double hydroxide nanosheet array. Inorganic Chemistry Frontiers 2023, 10 (9), 2766-2775.

43. Zhang, L.; Liang, J.; Yue, L.; Dong, K.; Li, J.; Zhao, D.; Li, Z.; Sun, S.; Luo, Y.; Liu, Q.; Cui, G.; Ali Alshehri, A.; Guo, X.; Sun, X., Benzoate anions-intercalated NiFe-layered double hydroxide nanosheet array with enhanced stability for electrochemical seawater oxidation. Nano Research Energy 2022.

44. Han, M. H.; Pin, M. W.; Koh, J. H.; Park, J. H.; Kim, J.; Min, B. K.; Lee, W. H.; Oh, H.-S., Improving the oxygen evolution reaction using electronic structure modulation of sulfur-retaining nickel-based electrocatalysts. Journal of Materials Chemistry A 2021, 9 (47), 27034-27040.

45. Li, H. B.; Yu, M. H.; Wang, F. X.; Liu, P.; Liang, Y.; Xiao, J.; Wang, C. X.; Tong, Y. X.; Yang, G. W., Amorphous ni ckel hydroxide nanospheres with ultrahigh capacitance and energy density as electrochemical pseudocapacitor materials. *Nat Commun* **2013,** *4*, 1894.

46. Wang, Z.; Liu, W.; Hu, Y.; Xu, L.; Guan, M.; Qiu, J.; Huang, Y.; Bao, J.; Li, H., An Fe-doped NiV LDH ultrathin nanosheet as a highly efficient electrocatalyst for efficient water oxidation. *Inorganic Chemistry Frontiers* **2019,** *6* (7), 1890-1896.

47. Wu, Y.; Xu, L.; Xin, W.; Zhang, T.; Cao, J.; Liu, B.; Qiang, Q.; Zhou, Z.; Han, T.; Cao, S.; Xiao, W.; Wei, J., Rational construction of 3D MoNi/NiMoOx@NiFe LDH with rapid electron transfer for efficient overall water splitting. *Electrochimica Acta* **2021,** *369,* 137680.

48. Li, T.; Lu, T.; Li, X.; Xu, L.; Zhang, Y.; Tian, Z.; Yang, J.; Pang, H.; Tang, Y.; Xue, J., Atomically Dispersed Mo Sites Anchored on Multichannel Carbon Nanofibers toward Superior Electrocatalytic Hydrogen Evolution. *ACS Nano* **2021,** *15* (12), 20032-20041.

49. Chang, C.; Chen, W.; Chen, Y.; Chen, Y.; Chen, Y.; Ding, F.; Fan, C.; Jin Fan, H.; Fan, Z.; Gong, C.; Gong, Y.; He, Q.; Hong, X.; Hu, S.; Hu, W.; Huang, W.; Huang, Y.; Ji, W.; Li, D.; Li, L.-J.; Li, Q.; Lin, L.; Ling, C.; Liu, M.; Liu, N.; Liu, Z.; Ping Loh, K.; Ma, J.; Miao, F.; Peng, H.; Shao, M.; Song, L.; Su, S.; Sun, S.; Tan, C.; Tang, Z.; Wang, D.; Wang, H.; Wang, J.; Wang, X.; Wang, X.; T. S. Wee, A.; Wei, Z.; Wu, Y.; Wu, Z.-S.; Xiong, J.; Xiong, Q.; Xu, W.; Yin, P.; Zeng, H.; Zeng, Z.; Zhai, T.; Zhang, H.; Zhang, H.; Zhang, Q.; Zhang, T.; Zhang, X.; Zhao, L.-D.; Zhao, M.; Zhao, W.; Zhao, Y.; Zhou, K.-G.; Zhou, X.; Zhou, Y.; Zhu, H.; Zhang, H.; Liu, Z., Recent Progress on Two-Dimensional Materials. *Acta Physico Chimica Sinica* **2021,** *0* (0), 2108017-0.

50. Yi, X.; Sun, H.; Robertson, N.; Kirk, C., Nanoflower Ni(OH)2 grown in situ on Ni foam for high-performance supercapacitor electrode materials. *Sustainable Energy & Fuels* **2021,** *5* (20), 5236-5246.

51. Dionigi, F.; Strasser, P., NiFe-Based (Oxy)hydroxide Catalysts for Oxygen Evolution Reaction in Non-Acidic Electrolytes. *Advanced Energy Materials* **2016,** *6* (23), 1600621.

52. Friebel, D.; Louie, M. W.; Bajdich, M.; Sanwald, K. E.; Cai, Y.; Wise, A. M.; Cheng, M. J.; Sokaras, D.; Weng, T. C.; Alonso-Mori, R.; Davis, R. C.; Bargar, J. R.; Norskov, J. K.; Nilsson, A.; Bell, A. T., Identification of highly active Fe sites in (Ni,Fe)OOH for electrocatalytic water splitting. *J Am Chem Soc* **2015,** *137* (3), 1305-13.

53. Chang, S.; Zhang, Y.; Zhang, B.; Cao, X.; Zhang, L.; Huang, X.; Lu, W.; Ong, C. Y. A.; Yuan, S.; Li, C.; Huang, Y.; Zeng, K.; Li, L.; Yan, W.; Ding, J., Conductivity Modulation of 3D‐Printed Shellular Electrodes through Embedding Nanocrystalline Intermetallics into Amorphous Matrix for Ultrahigh‐Current Oxygen Evolution. *Advanced Energy Materials* **2021,** *11* (28), 2100968.

54. Wang, C.; Yan, B.; Chen, Z.; You, B.; Liao, T.; Zhang, Q.; Lu, Y.; Jiang, S.; He, S., Recent advances in carbon substrate supported nonprecious nanoarrays for electrocatalytic oxygen evolution. *Journal of Materials Chemistry A* **2021,** *9* (46), 25773-25795.

55. Wang, N.; Ou, P.; Hung, S. F.; Huang, J. E.; Ozden, A.; Abed, J.; Grigioni, I.; Chen, C.; Miao, R. K.; Yan, Y.; Zhang, J.; Wang, Z.; Dorakhan, R.; Badreldin, A.; Abdel-Wahab, A.; Sinton, D.; Liu, Y.; Liang, H.; Sargent, E. H., Strong-Proton-Adsorption Co-Based Electrocatalysts Achieve Active and Stable Neutral Seawater Splitting. *Adv Mater* **2023,** *35* (16), e2210057.

56. Vanderbilt, D., Soft self-consistent pseudopotentials in a generalized eigenvalue formalism. *Phys Rev B Condens Matter* **1990,** *41* (11), 7892-7895.

57. Giannozzi, P.; Baroni, S.; Bonini, N.; Calandra, M.; Car, R.; Cavazzoni, C.; Ceresoli, D.; Chiarotti, G. L.; Cococcioni, M.; Dabo, I.; Dal Corso, A.; de Gironcoli, S.; Fabris, S.; Fratesi, G.; Gebauer, R.; Gerstmann, U.; Gougoussis, C.; Kokalj, A.; Lazzeri, M.; Martin-Samos, L.; Marzari, N.; Mauri, F.; Mazzarello, R.; Paolini, S.; Pasquarello, A.; Paulatto, L.; Sbraccia, C.; Scandolo, S.; Sclauzero, G.; Seitsonen, A. P.; Smogunov, A.; Umari, P.; Wentzcovitch, R. M., QUANTUM ESPRESSO: a modular and open-source software project for quantum simulations of materials. *J Phys Condens Matter* **2009,** *21* (39), 395502.

58. Hammer B, H. L. B., Nørskov J K., Improved adsorption energetics within density-functional theory using revised. *Physical review B* **1999,** *59* (11), 7413.

59. Cococcioni, M.; de Gironcoli, S., Linear response approach to the calculation of the effective interaction parameters in theLDA+Umethod. *Physical Review B* **2005,** *71* (3), 035105.

60. Nørskov, J. K., Rossmeisl, J., Logadottir, A., Lindqvist, L. R. K. J., Kitchin, J. R., Bligaard, T., & Jonsson, H., Origin of the Overpotential for Oxygen Reduction at a Fuel-Cell Cathode. *The Journal of Physical Chemistry B* **2004,** *108* (46), 17886-17892.

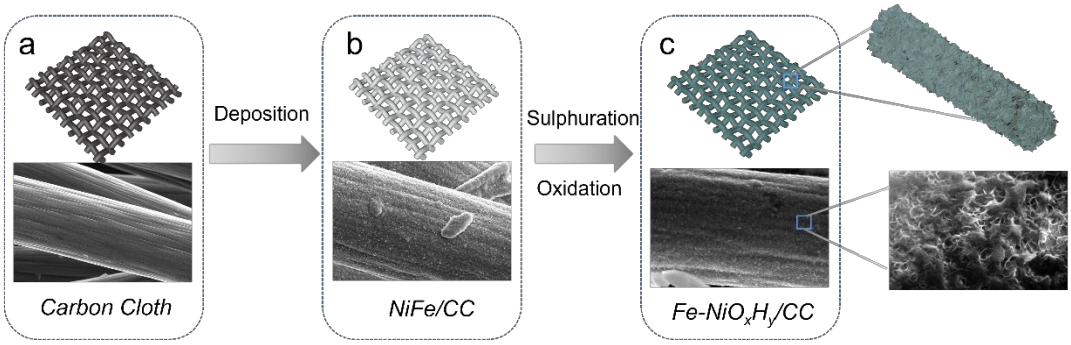

Figure 1. Schematic illusion of the synthesis of low Fe doping Ni-based catalyst on carbon cloth (Fe-NiO_xH_y/CC). (a) The conductive subtract of carbon cloth (CC), (b) Electrodeposited NiFe composites on carbon cloth (NiFe/CC), (c) As-prepared Fe-NiO_xH_y/CC after sulphuration and oxidation of NiFe/CC.

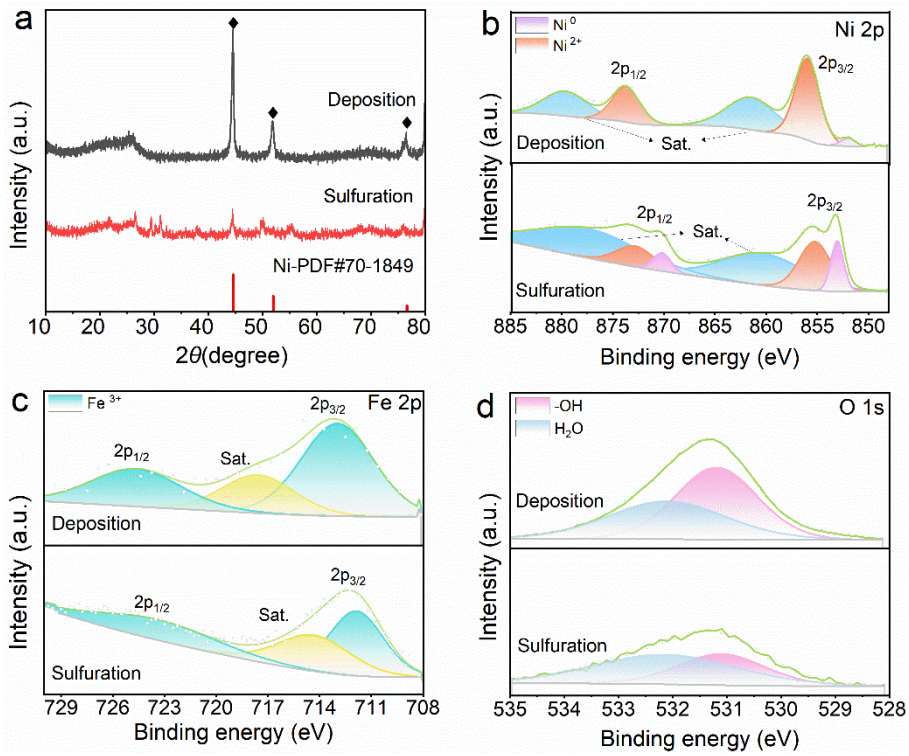

Figure 2. (a) XRD patterns of deposition and sulphuration of FeNi/CC. (b) Ni 2p, (c) Fe 2p, (d) O 1s High- resolution XPS spectrum for deposition and sulphuration of FeNi/CC.

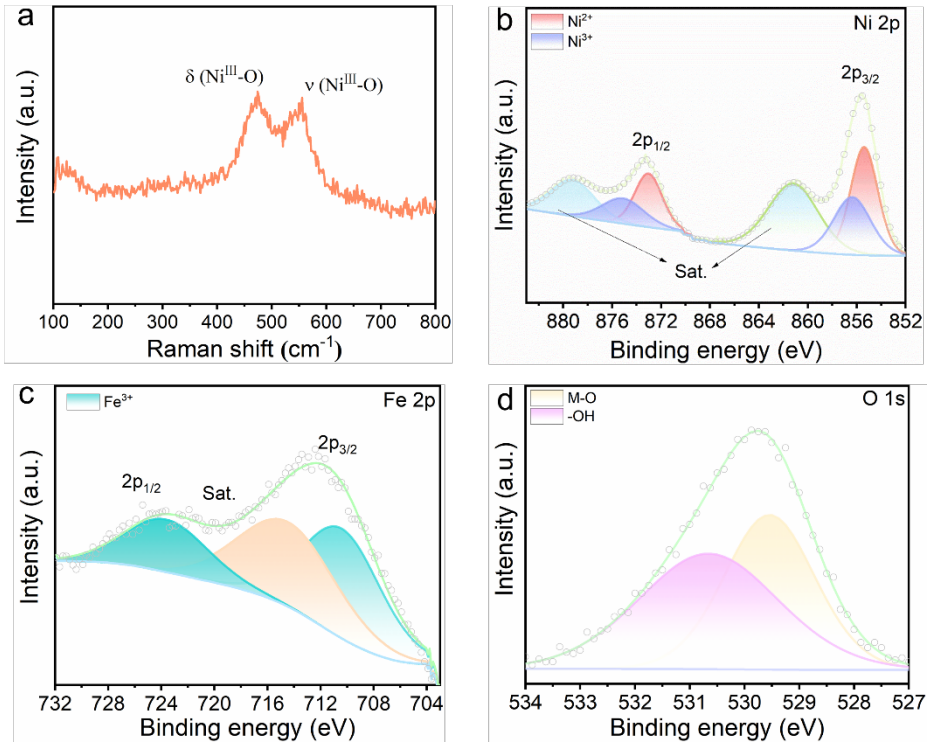

Figure 3. (a) Raman spectra of the Fe-NiO_xH_y/CC. (b) Ni 2p, (c) Fe 2p, (d) O1s high-resolution XPS spectra of the Fe-NiO_xH_y/CC.

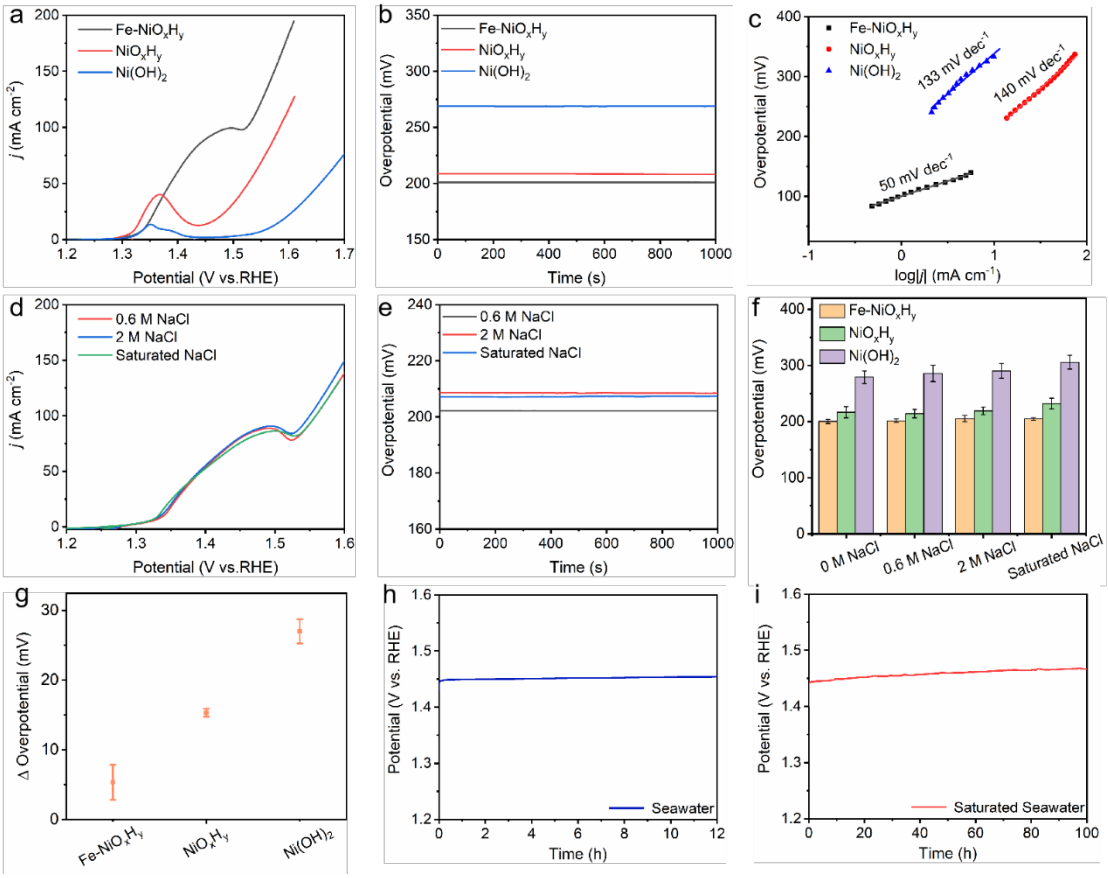

Figure 4. (a) Polarization curves (iR corrected) of Fe-NiO_xH_y/CC, NiO_xH_y/CC and $Ni(OH)_2$/CC in 1 M KOH electrolyte. (b) The chronopotentiometry measurement at a current density of 10 mA cm^{-2} for Fe-NiO_xH_y/CC, NiO_xH_y/CC and $Ni(OH)_2$/CC in 1 M KOH electrolyte. (c) Tafel plots of Fe-NiO_xH_y/CC, NiO_xH_y/CC and $Ni(OH)_2$/CC in 1 M KOH electrolyte. (d) Polarization curves (iR corrected) of Fe-NiO_xH_y/CC in the 0.6 M NaCl, 2 M NaCl and Saturated NaCl in 1 M KOH electrolytes. (e) The chronopotentiometry measurement at a current density of 10 mA cm^{-2} for Fe-NiO_xH_y/CC, in the 0.6 M NaCl, 2 M NaCl and Saturated NaCl in 1 M KOH electrolytes. (f) Corresponding histogram of overpotential for Fe-NiO_xH_y/CC, NiO_xH_y/CC and $Ni(OH)_2$/CC from 0 M to saturated salt in electrolyte at 10 mA cm^{-2}. (g) Overpotential difference against salt concentration gradient for Fe-NiO_xH_y/CC, NiO_xH_y/CC and

$Ni(OH)_2$/CC. (h) The chronopotentiometry measurement at a current density of 10 mA cm^{-2} for the Fe-NiO_xH_y/CC. in seawater (i) The chronopotentiometry measurement at a current density of 10 mA cm^{-2} for the Fe-NiO_xH_y/CC in saturated seawater. (All polarization curves were measured by LSV at scan rate of 1 mV s^{-1}.)

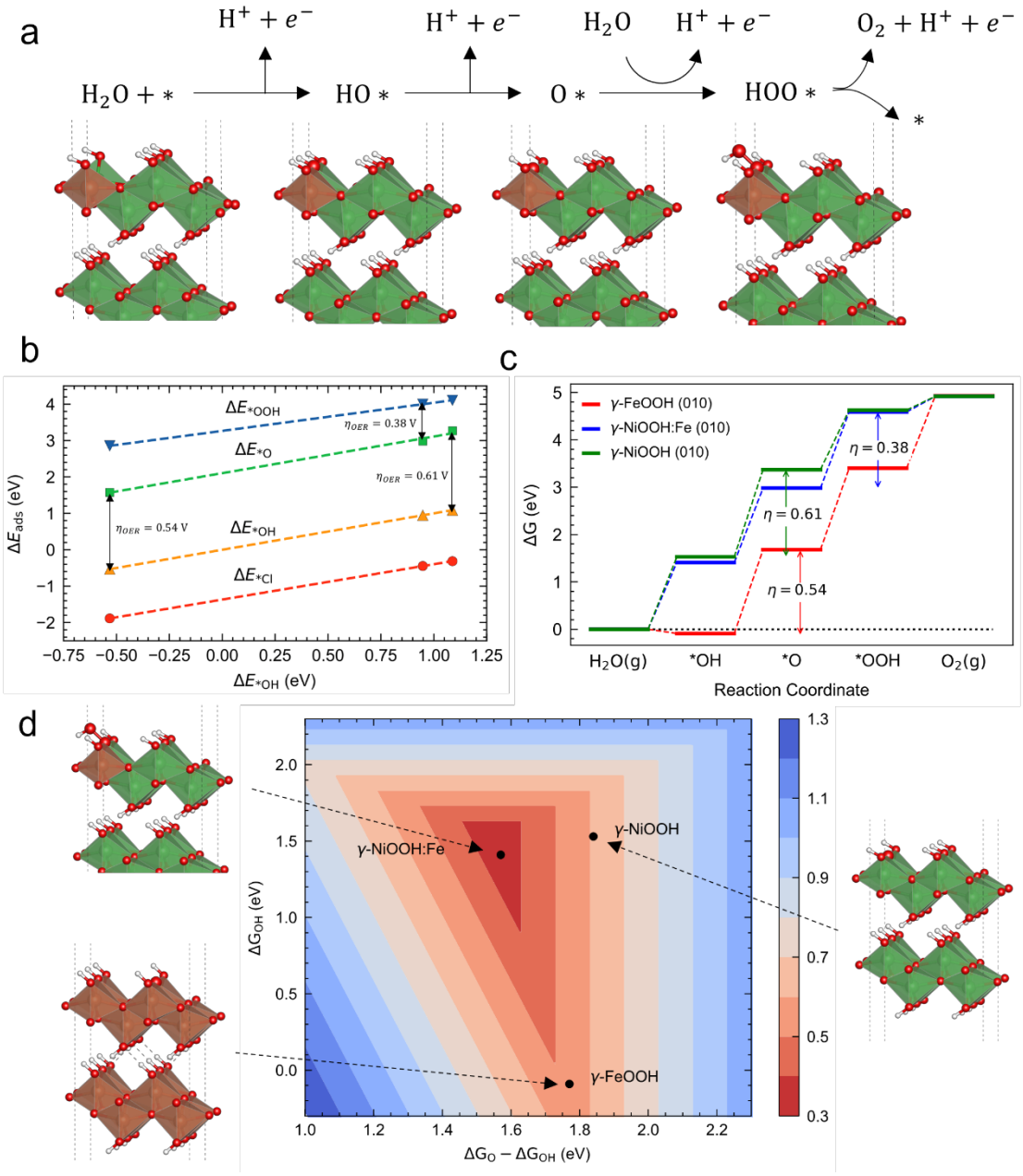

Figure 5. (a) The proposed OER pathway on the (010) surface of Fe-NiO_xH_y/CC models, where the red and green octahedrons represent Fe and Ni atoms, respectively. (b) Computed adsorption energies of OER and Cl* intermediates, (c) theoretical OER free energy diagram for the pure NiOOH, FeOOH and Fe-doped NiOOH. (d) Two-dimensional OER activity volcano representing the overpotentials as a function of Gibbs free energies of OER intermediates.

Table of Contents Graphic

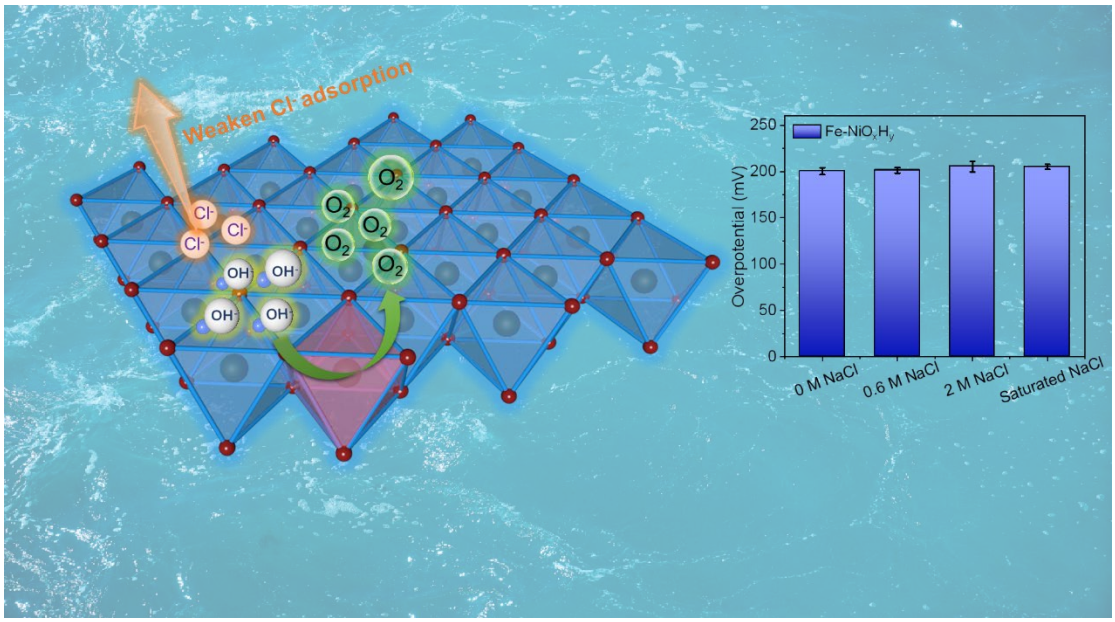

Low doping concentration of iron in the nickel oxyhydroxide can reduce chloride ion adsorption while enhancing the oxygen evolution reaction activity, which leads to stable catalytic activity from 0 M to saturated alkaline salt electrolyte.